Development of High Detection Efficiency Titanium Transition-Edge Sensors for 1550 nm Single-Photon Detection

Development of High Detection Efficiency Titanium Transition-Edge Sensors for 1550 nm Single-Photon Detection

Abstract

Transition-edge sensors (TESs) have shown the capability of both energy resolution and resolving photon numbers. In this work, we present the fabrication and characterization of high detection efficiency Ti optical TESs with the critical temperature T_c = 213 mK and the photon-number resolving capability at telecommunication wavelength 1550 nm. The Ti superconducting film is prepared by a DC magnetron sputtering technique. An optical cavity comprised of 5-layers antireflection and 15-layers high-reflection Ta_2O_5/SiO_2 is enclosed with the Ti film by an ion beam assisted deposition method to improve detection efficiency, which brings the absorption of 99.74%. The energy resolution for the Ti TES with sensitive area 20 μm × 20 μm is 0.45 eV and the detection efficiency is 97% ± 1%.

Introduction

Superconducting photon-number-resolving detectors (SPNRDs) are now applied in the quantum optics and quantum information fields worldwide [1], [2], [3], [4], [5], [6]. Several types of SPNRDs have been proposed such as microwave kinetic inductance detectors (MKIDs) [7], superconducting nanowire single-photon detectors (SNSPDs) [8], and superconducting transition-edge sensors (TESs) [9].

When SPNRDs act as core components in quantum information applications, they must concurrently achieve several critical performance metrics: high energy resolution [10], low dark count rates [3], minimal timing jitter [11], and near-unity quantum detection efficiency [12].

Quantum detection efficiency is especially crucial in the single photon metrology. AIST demonstrated an overall system efficiency of 98% at 850 nm [13]. NIST reported system detection efficiency of 95% at 1550 nm [14], and Purple Mountain Observatory recently also achieved that of 95% at 1550 nm [15]. Although superconducting nanowire single-photon detectors (SNSPDs) have achieved 98% detection efficiency at 1550 nm [16], the detector's fidelity to the photon-number state collapses rapidly as the photon number increases [17]. Consequently, TES detectors remain the most promising candidate for high-accuracy photon-number-resolving metrology.

We have been developing Ti TESs with high quantum efficiency, which delivers the energy resolution required for quantum information applications. In this work, we report on the optical characterization of these devices, with a particular focus on the photon-number statistics and the system detection efficiency (SDE).

Fabrication of Ti TESs

A 15-layer Ta_2O_5/SiO_2 distributed Bragg reflector (DBR) [18] is deposited directly onto the silicon substrate beneath the entire device. The Ti-sensitive element and Nb superconducting leads are subsequently patterned using UV lithography, deposited via DC magnetron sputtering [19], and defined by lift-off. [19], and defined by lift-off. A five-layer Ta_2O_5/SiO_2 anti-reflection (AR) coating is then deposited on the center area of the TESs through a shadow mask.

The micrograph in Fig. 1 shows a Ti TES device; concentric diffraction rings from the DBR-TES-AR stack are clearly visible.

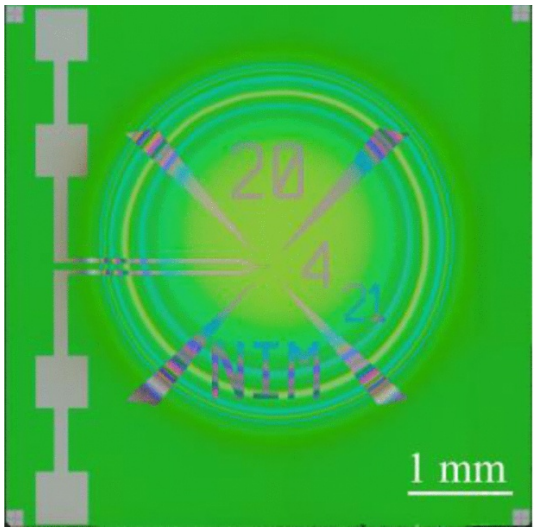

Fig. 1: *Optical micrograph of the Ti TES device showing concentric diffraction rings from the anti-reflection cavity.*

Table I summarizes the parameters of the TESs: the thickness of the Ti film, critical temperature (T_c), transition width (ΔT_c), and the effective sensitive area (A_s). The TES was characterized by a four-wire configuration using an ac resistance bridge. A 1-μA excitation current was applied. The resistance–temperature (R–T) curve is shown in Fig. 2, the hysteresis loop arises from two factors: (i) self-heating effects during upward and downward sweeps of the $R(T)$ transition curves [20], and (ii) imperfect thermal contact between the TES device substrate and Cu plate [21]. T_c be determined from the heating scan, thus the critical temperature T_c = 213 mK and the transition width ΔT_c = 4.1 mK. The normal resistance R_n is 23 Ω.

TABLE I The Parameters of a Ti TES

Ti Thickness/nm	T_c/mK	ΔT_c/mK	A_s/μm^2
20	213	4.1	20×20

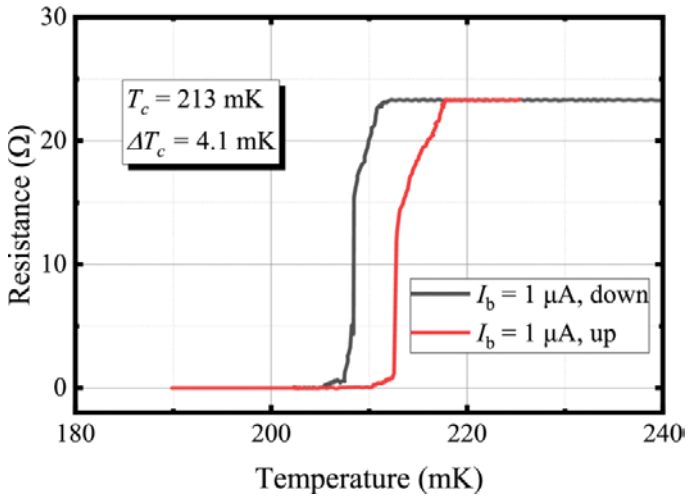

Fig. 2: *The R–T curve of the TES device.*

The active area of 20 × 20 μm^2 exceeds the mode-field diameter of the UHNA-3 fiber, so the fiber-to-TES alignment is straightforward. The heat capacity is calculated from the Ti thickness and effective sensitive area, and the resulting theoretical energy resolution ΔE [22] which is sufficient to resolve individual 1550-nm photon.

Fig. 3 shows the measured absorption of the DBR-TES-AR stack, which is a 4-inch wafer upon which the DBR-TES-AR optical structure has been deposited without UV lithographic patterning [9], which could recorded with a Horiba UVISEL2 spectroscopic ellipsometer. Inset: TF-Calc, an optical thin film coating simulator [13], prediction versus experimental result for the same layer sequence; the design band is centered at 1550 nm with 40 nm waveband. The absorption at 1550 nm reaches 99.8% in the model and spectroscopic ellipsometer record 99.74% at room temperature; the offset is attributed to minor thickness and refractive-index deviations in the SiO_2/Ta_2O_5 multilayer.

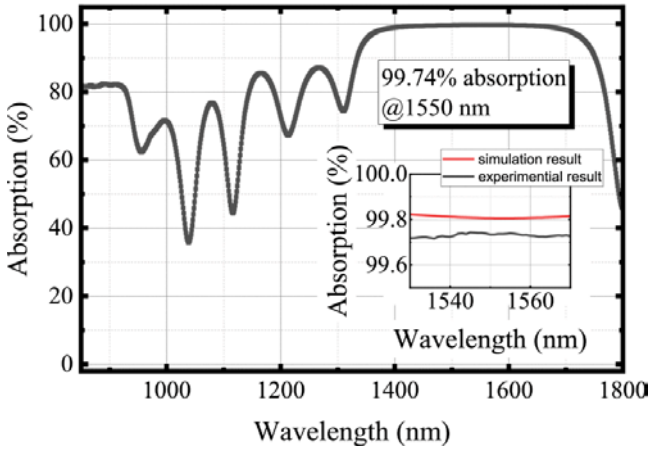

Fig. 3: *Absorption of the DBR-TES-AR optical cavity. In the inset, a comparison is presented between the simulation (red line) and the measurement (black line) in the design region.*

Single Photon Detection Results

The TES die is anchored to the 30 mK mixing chamber stage of a dry dilution refrigerator. A zirconia-ferruled UHNA-3 fiber (mode-field diameter 4.1 μm, NA 0.35) is brought to the pixel with a micrometer-resolution stage, in previous work [15]. To eliminate Fresnel loss, index-matching fluid (n = 1.58) fills the gap between the cleaved facet and the AR-coated surface. The fiber pigtail is connected to an attenuated pulsed diode laser (HAMAMATSU C10196 picosecond light pulser, λ = 1549.79 nm, 37 ps pulse width, 20 kHz repetition rate). Photon number per pulse is set by variable attenuation.

Commercial optical-power heads use InGaAs avalanche photodiodes (InGaAs APDs) with a noise floor of ≈10 pW (Keysight N7752A 2-channel optical attenuator with integrated power meters, calibrated at NIM (Cert. No. GXgf2024-06927).) three orders of magnitude above the single-photon regime of our TES (Fig. 4).

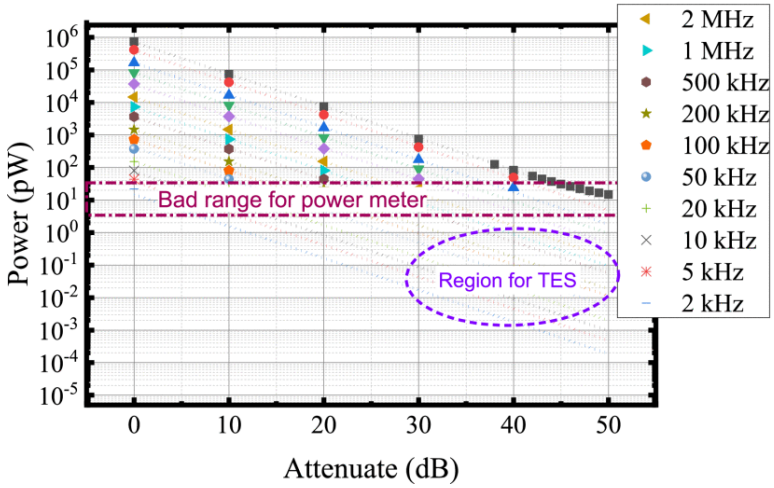

Fig. 4: *Optical power detection range of commercial power meter and TES.*

At high repetition rate or low attenuation, the APD read-out remains reliable, once the average power approaches 10 pW the signal is buried by dark counts and the displayed value drifts. To bridge the four-decade gap between the APD limit (10 pW) and the TES sensitivity (≈0.1 fW) we implemented a relay chain of two variable attenuators (VAs) and two channels power meter (PMs) (calibrated Keysight N7752A) that preserves an unbroken traceability of the photon flux.

Fig. 5. Schematic of the optical quantum-efficiency setup. Two variable attenuators (VA1, VA2) and two power meters (PM1, PM2) are arranged so that the laser first passes through VA1, a 99:1 fiber splitter, PM1, VA2, and finally PM2. Calibration proceeds in two stages. (i) Split-ratio measurement: VA1 is set to 0 dB and VA2 to ~17 dB, well above the APD floor; the ratio R_{PM} is recorded for >100 shots and averaged. R_{PM} is defined as P_{PM2} / P_{PM1}. (ii) Single-photon operation: VA1 is driven to 10–20 dB and the pulse repetition rate reduced to f = 20 kHz, bringing the average power at PM1 into the 0.1–1 nW range. The input photons per pulse (μ_{in}) is obtained by following equations:

$$\mu_{in} = P_{PM1} \times \frac{R_{PM}}{fh\upsilon} \qquad (1)$$

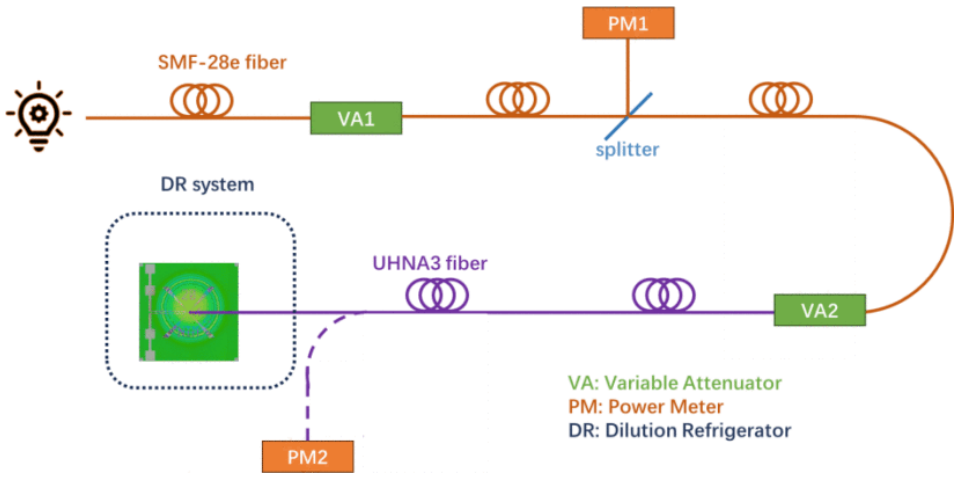

Fig. 5: *Experimental setup. SMF-28e fiber (orange) links the laser to VA2; UHNA-3 fiber (purple) connects VA2 to the TES.*

P_{PM1} is the power measured by PM1, R_{PM} is the split ratio carried over from step (i), f is the laser repetition rate, h is Planck's constant, and υ is the optical frequency at 1550 nm.

In the experiment, UHNA-3 fiber that delivers the attenuated photon flux to the TES is connected to VA2 via a fiber-optic connector; VA2, in turn, is directly connected to the SMF-28e patch cord attached to the 99:1 monitor tap. Each joint introduces a well-characterized loss of 0.15–0.25 dB, dominated by the mode-field mismatch between the 1.8 μm UHNA-3 core and the 8.2 μm SMF-28e core [23]. This loss, together with the 20 dB splitter ratio and any additional connector or fusion-splicing losses, is included in the R_{PM} calibration spreadsheet. Propagating these terms through the chain anchors the absolute photon flux at the TES to the traceable power recorded by PM1—something a stand-alone VA/PM system cannot provide.

Amplitude histograms are plotted and shown in Fig. 6, acquired with a 200 kHz low-pass filter engaged during photon counting, a Poisson distribution is observed for the amplitudes of these peaks. The extracted means output photon number μ_{out} = 0.8 photons per pulse. The corresponding energy resolution, defined as the full-width at half-maximum of the photon-energy peak, is ΔE = 0.45 eV.

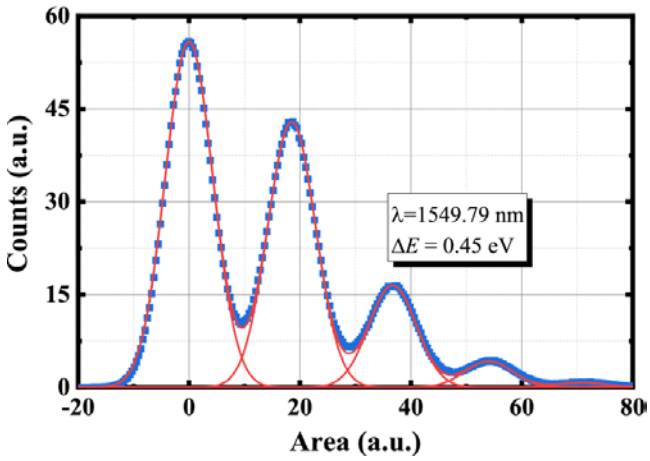

Fig. 6: *Amplitude histogram shows four photon-number states for TES.*

By systematically adjusting variable attenuator VA1, we record a continuous family of Poisson-distributed amplitude histograms. The overall line attenuation is reduced in fine, calibrated steps from 54 dB down to 46 dB, causing the mean output photon number per pulse, μ_{out}, to climb reproducibly from 0.8 to 7.6 photons (Fig. 7). At every step, the 0-, 1-, 2-, … photon-state peaks remain well-resolved Gaussians (Fig. 6), permitting peak-by-peak fitting. By systematically varying the attenuation setting of VA1, the overall link loss is altered in a controlled, stepwise fashion; in this way, a complete sequence of mean photons-per-pulse values is obtained as the attenuation is progressively changed.

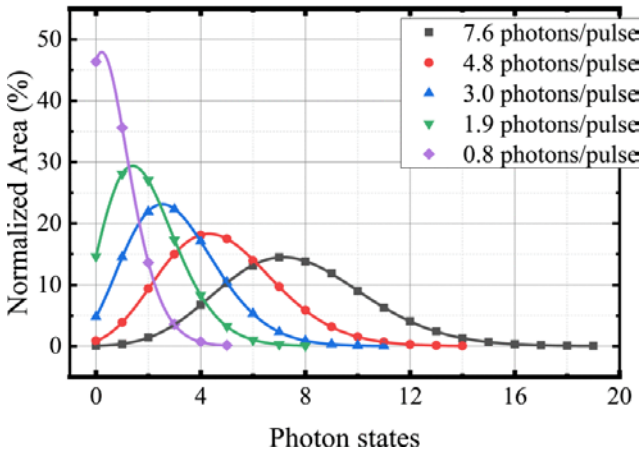

Fig. 7: *Poisson-distributed amplitude histograms obtained by varying the optical attenuator.*

For the detection-efficiency measurement we define $\eta = \mu_{out}/\mu_{in}$, where μ_{out} is the mean photons per pulse registered by the TES and μ_{in} is the mean photons per pulse inferred from the calibrated monitor power meter. Fig. 8 plots μ_{out} versus μ_{in} while the variable attenuator is scanned; a linear fit to the data yields a slope of 0.970 ± 0.001. Type B uncertainty (0.87%, k = 2) is dominated by the power meter (0.0088% contribution from splitting ratio calculation). Adding Type A uncertainty (0.20%, k = 2) gives a combined relative uncertainty of 0.89% (k = 2), rounded to ~1%. The resulting system detection efficiency is 97% ± 1%.

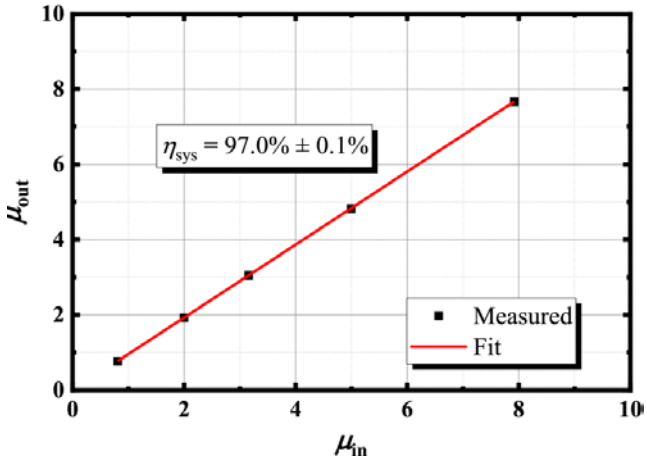

Fig. 8: *The detected mean photons vs the input mean photons.*

Conclusion

The optical Ti-TES achieves 0.45 eV energy resolution over a 20 × 20 μm^2 active area and exhibits a system detection efficiency of 97% ± 1%. These combined capabilities—high energy resolution and wide photon-number dynamic range—position the TES as a promising sensor for single-photon-source evaluation and optical quantum metrology.

References

1. A. Meda, I. Pietro Degiovanni, A. Tosi, Z. Yuan, G. Brida, and M. Genovese, “Quantifying backflash radiation to prevent zero-error attacks in quantum key distribution,” *Light Sci. Appl.*, vol. 6, no. 6, Jun. 2017, Art. no. e16261.

2. S. Yang, L. You, M. Zhang, and J. Wang, “Research of single photon detectors applied in quantum communication,” *Inform. Manage. Sci. IV*, vol. 205, pp. 19–27, 2013.

3. L. Manenti et al., “Dark counts in optical superconducting transition-edge sensors for rare-event searches,” *Phys. Rev. Appl.*, vol. 22, no. 2, 2024, Art. no. 024051.

4. P. Szypryt et al., “Kinetic inductance current sensor for visible to near-infrared wavelength transition-edge sensor readout,” *Commun. Eng.*, vol. 3, 2024, Art. no. 160.

5. T. Jodoi, T. Tsuruta, M. Rajteri, and D. Fukuda, “Evaluation of detection efficiency of a transition edge sensor at C-band wavelength,” *Opt. Laser Technol.*, vol. 192, 2025, Art. no. 113414.

6. T. Konno, S. Takasu, K. Hattori, and D. Fukuda, “Development of an optical transition-edge sensor array,” *J. Low Temp. Phys.*, vol. 199, no. 1–2, pp. 27–33, 2020.

7. N. Zobrist et al., “Wide-band parametric amplifier readout and resolution of optical microwave kinetic inductance detectors,” *Appl. Phys. Lett.*, vol. 115, no. 4, 2019, Art. no. 042601.

8. G. He et al., “Simultaneous resolution of photon numbers and positions with series-connected superconducting nanowires,” *Appl. Phys. Lett.*, vol. 120, no. 12, Mar. 2022, Art. no. 124001.

9. X. Xu et al., “Development of Ti/Au transition-edge sensors for single-photon detection,” *IEEE Trans. Appl. Supercond.*, vol. 34, no. 3, May 2024, Art. no. 2100104.

10. K. Hattori, T. Konno, Y. Miura, S. Takasu, and D. Fukuda, “An optical transition-edge sensor with high energy resolution,” *Supercond. Sci. Technol.*, vol. 35, no. 9, Sep. 2022, Art. no. 095002.

11. A. McCarthy et al., “High-resolution long-distance depth imaging LiDAR with ultra-low timing jitter superconducting nanowire single-photon detectors,” *Optica*, vol. 12, no. 2, pp. 168–177, 2025.

12. K. Hattori, S. Inoue, R. Kobayashi, K. Niwa, T. Numata, and D. Fukuda, “Optical transition edge sensors : Wavelength dependence of system detection efficiency,” in *Proc. Conf. Precis. Electromagn. Meas.*, 2018, pp. 1–2.

13. D. Fukuda et al., “Titanium-based transition-edge photon number resolving detector with 98% detection efficiency with index-matched small-gap fiber coupling,” *Opt. Exp.*, vol. 19, no. 2, pp. 870–875, Jan. 2011.

14. A. E. Lita, A. J. Miller, and S. W. Nam, “Counting near-infrared single-photons with 95% efficiency,” *Opt. Exp.*, vol. 16, no. 5, pp. 3032–3040, 2008.

15. P. Li et al., “High-performance Ti transition-edge sensor-based photon-number resolving detectors,” *J. Low Temp. Phys.*, vol. 214, no. 3–4, pp. 100–105, 2024.

16. D. V. Reddy, R. R. Nerem, S. W. Nam, R. P. Mirin, and V. B. Verma, “Superconducting nanowire single-photon detectors with 98% system detection efficiency at 1550 nm,” *Optica*, vol. 7, no. 12, pp. 1649–1653, Dec. 2020.

17. Z. Shu et al., “On-chip superconducting nanowire single-photon detectors integrated with pump rejection for entanglement characterization,” *Photon. Res.*, vol. 13, no. 4, pp. 1067–1073, 2025.

18. A. E. Lita, D. V. Reddy, V. B. Verma, R. P. Mirin, and S. W. Nam, “Development of superconducting single-photon and photon-number resolving detectors for quantum applications,” *J. Lightw. Technol.*, vol. 40, no. 23, pp. 7578–7597, Dec. 2022.

19. X. Xu et al., “Investigation of superconducting Ti/Ti-Au/Au tri-layer films with a co-sputtering process for transition-edge sensors,” *IEEE Trans. Appl. Supercond.*, vol. 33, no. 5, Aug. 2023, Art. no. 1102005.

20. M. L. Ridder et al., “Study of TES detector transition curve to optimize the pixel design for frequency-division multiplexing readout,” *J. Low Temp. Phys.*, vol. 199, no. 3–4, pp. 962–967, 2020.

21. D. Vaccaro et al., “Tuning the TC of titanium thin films for transition-edge sensors by annealing in argon,” *J. Low Temp. Phys.*, vol. 193, no. 5–6, pp. 1122–1128, 2018.

22. L. Lolli, E. Taralli, M. Rajteri, T. Numata, and D. Fukuda, “Characterization of optical fast transition-edge sensors with optimized fiber coupling,” *IEEE Trans. Appl. Supercond.*, vol. 23, no. 3, Jun. 2013, Art. no. 2100904.

23. J. W. Henke et al., “Integrated photonics enables continuous-beam electron phase modulation,” *Nature*, vol. 600, no. 7890, pp. 653–658, 2021.